Measuring relative energies of ligand binding conformations on nanocluster surfaces with temperature-dependent FTIR spectroscopy

*Megan D. Klein[‡], Casey H. Bisted[‡], Florence Y. Dou, Jason W. Sandwisch, Brandi M. Cossairt, Munira Khalil**

AUTHOR ADDRESS

Department of Chemistry, University of Washington, Seattle, Washington 98195, United States

KEYWORDS Nanoclusters, Nanocrystals, InP, Ligand, Binding Geometries, Conformation Energy

ABSTRACT

We present a method to measure relative energies between binding conformations of carboxylate ligands on InP magic-sized clusters dissolved in solution. Using Markov Chain Monte Carlo global fitting analysis on temperature-dependent vibrational spectra of cluster-bound ligands, we observe significantly different relative energies between various bidentate and monodentate binding motifs. Relative to the monodentate motif, the chelating conformation is 0.7 ± 0.3 kcal/mol more stable, the *syn-syn* bridging conformation is 1.1 ± 0.5 kcal/mol more stable, but the *syn-anti* bridging conformation exhibits no significant difference. Our results find that the relative energy between monodentate-bound carboxylates and unbound carboxylic acids is 4.52 ± 0.05 kcal/mol, or 1582 ± 19 cm^{-1}, nearly identical to the carboxylate asymmetric stretching frequency. We suggest that the ligand vibrational energy may play a key role in ligand dissociation by compensating for energy differences between bound and dissociated ligand states. This approach gives important experimental insights into ligand binding and can inform future nanocrystal surface engineering.

INTRODUCTION

In recent years, semiconductor nanocrystal (NC) materials have demonstrated their utility across a range of optoelectronic applications. The emissive properties of these NCs have proven highly advantageous in the areas of light emitting diodes[1,2] and lasing,[3–5] while their absorptive behavior has led to their use in luminescent solar concentrators and numerous other photovoltaic and photocatalytic applications.[6–12] In particular, the size-tunability, narrow emission linewidths, strong absorption, and high quantum yield of nanomaterial platforms are desirable properties for numerous types of devices. Recent work has even begun investigating the potential for colloidally synthesized NCs to be utilized as photon sources in quantum information applications.[13–15] In order to ensure these materials can be utilized to their fullest extent, it is crucially important to have a fundamental understanding of the properties that dictate NC photophysics.

While the core of a NC determines many of its characteristic photophysical properties, these properties are often highly sensitive to disruption by defects at the surface of the NC. It has been shown that undercoordinated surface anions are a predominant cause of sub-bandgap trap states that localize charges and dominate exciton recombination.[16–23] Due to this effect of surface anions, many NC syntheses are performed with an excess of cation precursors to ensure a cation-rich surface.[24,25] In addition, capping ligands are typically incorporated on the nanomaterial surface, playing a multifaceted role of passivating dangling surface bonds, ensuring charge balance, and promoting particle stability (both chemical and colloidal). Given the critical impact these ligands have on preserving NC properties, they are a subject of significant and continued study in the field.[26–29] Numerous classes of both organic and inorganic ligands are used to functionalize nanocrystal surfaces. Organic ligands with long alkyl tails are a common example as they ensure surface passivation, prevent particle agglomeration, and enable NC suspension in

organic solvents. These alkyl tails are frequently used in conjunction with carboxylate head groups, which act as X-type ligands: covalently bonding to surface cations, while also ensuring charge balance at the nonstoichiometric surface.[30–32] Despite the covalent ligand-NC bond, the ligand shell has been shown to be dynamic with frequent self-exchange aided by solvent, excess ligand, or elevated temperatures.[33–35]

To probe the dynamic nature and energetics of nanocrystal-bound ligands, previous studies have often relied on ligand exchange reactions. By monitoring the displacement of one ligand species following the addition of a second, information can be obtained on the difference in free energies between the types of ligands.[36–43] While these experiments are indisputably valuable in understanding binding differences between ligand species, they are unable to give insights into differences between binding motifs of a single species. In the case of carboxylate-capped InP nanocrystals, previous work by Gary et al. has shown that four different binding geometries can be observed via single crystal X-ray diffraction, with a fifth monodentate geometry observed in NMR studies.[41,44] There is much motivation to understand differences in binding motifs since they may also affect the surface reactivity and kinetics of nanocrystal growth, ultimately impacting factors such as shape and size dispersity for high-quality NCs.[45] However, unlike ligand displacement reactions, there is no easy handle by which to titrate between these binding motifs, making it very difficult to gain information about energetics between these configurations.

Several studies have used computational methods to calculate binding energies of ligand head groups on NC surfaces. Many of these have focused on L-type ligands that form a dative bond to the surface by donating an electron pair, including those with a protonated carboxylic acid head group.[46,47] However, it has been shown that with carboxylic acid ligands, the predominant binding species to II-VI and III-V semiconductor NCs is the aforementioned conjugate carboxylate

anion.[35,41,48,49] Furthermore, of the computational studies investigating carboxylate species, many focus on the binding of the MX_2 complex formed by a metal ion and two X-type ligands, such as the cadmium oleate complex $Cd(OA)_2$, which itself can act as a Z-type ligand and accept an electron pair from a surface anion.[50,51] While MX_2 ligands can be readily displaced via substitution with an L-type ligand,[24] in some systems such as InP magic-sized clusters (MSCs), it has been shown that metal ions are not displaced from the surface until well above 100 °C.[34] Despite this, the ligands are observed exchanging well below this temperature, meaning that the carboxylate species themselves are dynamically rearranging or dissociating from the surface.[34] Work by Xie et al. calculated the relative energies involved in rearrangement of carboxylate ligands in clusters of indium acetate complexes and found values ranging from 0-3 kcal/mol for converting between chelating and bridging conformations, and around 15-20 kcal/mol for converting between chelating and monodentate.[52] However, both of these values were strongly dependent on the surrounding environment of In atoms and ligand molecules and we would expect them to change drastically when going from an indium acetate cluster to the surface of an InP MSC. A study by Zhang et al. looked to calculate the binding energy of carboxylate moieties on facets of CdSe NCs and found a significantly larger difference of 50-80 kcal/mol between chelating and bridging conformations.[53] In the limit of low ligand density this relative energy difference decreased to 3 kcal/mol, which is much closer to the results calculated for the indium acetate clusters. While these computational results have generated some insight into the surface energetics of these binding motifs, there remains an urgent need for experimental measurements.

In this work, we present a temperature-dependent Fourier transform infrared (FTIR) spectroscopy method to study evolving populations of binding configurations for myristate-capped InP magic-sized clusters and extract relative energy differences between them. By utilizing the

variation in the asymmetric COO^- stretching frequencies between binding motifs, we globally fit the series of spectra to a set of five gaussian peaks across all temperatures via a Markov Chain Monte Carlo (MCMC) process. We then used the changes in peak areas to find the relative energy differences between the binding configurations of carboxylate groups, as well as the free carboxylic acid species. From these results, we observe that the energetic separation between a monodentate ligand and a free ligand is approximately equal to the vibrational stretching frequency of the carboxylate group. This strongly suggests a connection between vibrational excitation of the ligand and its dissociation from the surface. Additionally, we observe that the difference between bidentate and monodentate can be far smaller - and for some bidentate configurations the additional bond may not provide any increased stability at all. This experimental approach enables measuring energy differences between binding motifs, offers unique insight into NC surface energetics, and further suggests that the ligand shell may be even more dynamic than previously thought.

METHODS

InP MSC Synthesis and Characterization

Indium phosphide magic-sized clusters were prepared following the previously reported procedure.[44] A 100 mL 3-neck round bottom flask was charged with 0.936 g indium acetate (3.2 mmol, 1 eq) and 2.66 g myristic acid (11.5 mmol, 3.6 eq), and heated at 105 °C overnight with stirring under vacuum. The resulting indium myristate was then dissolved in 20 mL anhydrous toluene. In a nitrogen filled glovebox, 500 µL of $P(SiMe_3)_3$ (1.72 mmol, 0.54 eq) was added to 10 mL anhydrous toluene and the solution transferred to a syringe. The contents were rapidly injected into the reaction flask. The reaction then proceeded at 105 °C until no further changes were observed by UV-Vis (Cary Agilent 500), about 50 min. The MSCs were then cooled and the

toluene removed by vacuum distillation. The clusters were brought into the glovebox and redissolved in toluene and precipitated with acetonitrile. This was repeated for a minimum of three rounds of precipitation. One final spin was done in pentane alone as the solvent to remove any undissolved species. The clusters were purified by size exclusion chromatography over 4 Å molecular sieves in toluene and stored dry as a waxy solid.

FTIR Measurements

FTIR measurements were conducted in a Jasco 4100 FTIR spectrophotometer under a positive pressure of N_2. An 8 mg/mL solution of MSCs was flowed through a liquid cell with a 300 μm Teflon spacer. Heated measurements were conducted with a temperature controlled demountable liquid cell (Harrick) paired with a Peltier heater at 1 °C/min. The sample was left to equilibrate for 10 minutes at each temperature point. Flowing was stopped when recording spectra and then resumed to ensure thermal equilibrium.

Markov Chain Monte Carlo Sampling

A homebuilt sampling algorithm was constructed in Python 3.8 following the parallelizable walker update scheme laid out by Foreman-Mackey et al.[54] Affine invariant sampling was used in the form of the stretch move described by Goodman and Weare.[55] A prior distribution was constructed based off a room temperature fit of the InP MSC FTIR spectrum (Fig. S3), with standard deviations equal to those of the fit parameters. Following a proposed step, the predicted spectrum was generated by least squares fitting the amplitude of the five gaussian peaks, corresponding to the proposed point in parameter space, to the FTIR spectrum at each temperature point. The log likelihood was then calculated as the negative sum of squared residuals. In order to ensure the assumption of normally distributed error was met, the fits and data were converted to

transmission prior to calculating the residuals. Chains were thinned down to every 10 steps, and runs were typically performed with 200 walkers and a total of ~300,000 proposed moves. The acceptance proportion was kept between 0.2 and 0.4 by adjusting the step size of the stretch move prior to a run if needed. The correlation plot for the parameters is shown in Fig. S4. The elliptical distributions of all of the peak parameter correlations demonstrate adequate parameterization of the model. Additionally, the results with the given prior distribution were validated by performing the MCMC global fitting again using wider prior distributions, as well as once more with uninformed priors. The results for these runs are shown in Figs. S5-S8 and compared in Tables S1 and S2. Importantly, while we observe an increase in the uncertainty moving to wider and then uninformed prior distributions, we do not see a significant change in the extracted parameters or relative energies.

RESULTS AND DISCUSSION

To study the energetics of carboxylate ligand binding modes on NC surfaces, we used myristate-capped InP magic-sized clusters, which have a precisely known formula and structure allowing for more rigorous analysis than larger and more heterogeneous nanoparticles. The physical structure of the phenylacetate variant of these MSCs was characterized via single crystal X-ray diffraction and the electronic structure was probed using UV-Vis spectroscopy (Fig. S1). While the MSC consists of a nearly stoichiometric $[In_{21}P_{20}]^{3+}$ core, the surface is cation rich and exhibits a dense and interconnected indium carboxylate ligand network,[44] resulting in a molecular formula of $In_{37}P_{20}(O_2CR)_{51}$ where, in this case, R represents the myristate alkyl tail, $C_{13}H_{27}$.[41,56] Because fifty-one X-type carboxylate ligands are stoichiometrically bound to the InP MSC core for charge stabilization[34,41], surface ligand density cannot be synthetically tuned without changing the chemical identity of the MSC. However, in the presence of free carboxylic acid, L-type

adsorption of carboxylic acids on MSCs accounts for up to 15% of the ligated species[41,57] - impacting surface saturation.

Figure 1 plots the temperature-dependent FTIR spectra of the carboxylate vibrations of the bound (1400-1600 cm^{-1}) and free (1700-1780 cm^{-1}) myristate ligands. The bidentate nature of the carboxylate head group gives rise to five surface ligand binding motifs – chelating, syn-anti and

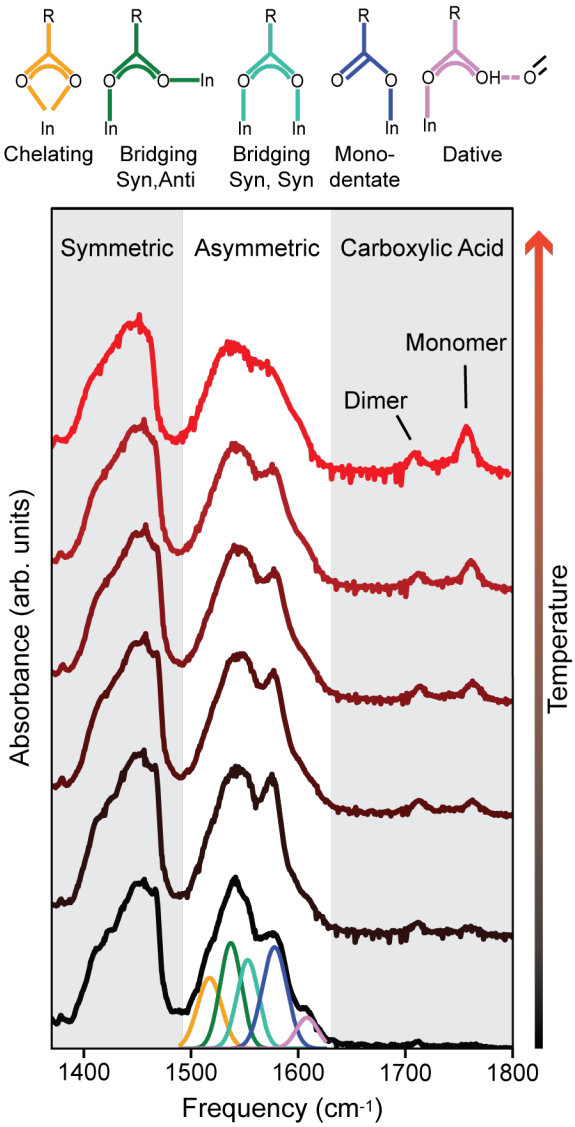

Figure 1. Representative FTIR spectra from the temperature-dependent measurement of myristate-capped InP MSCs spanning from 25 °C (bottom) to 100 °C (top) in increments of 15 °C and demonstrating changes that occur with increasing temperature along with peak assignment of asymmetric carboxylate stretching region. From left to right, binding groups shown include chelating (yellow), bridging *syn-anti* (green), bridging *syn-syn* (light blue), monodentate (dark blue), and dative (pink).

syn-syn bridging, monodentate, and dative illustrated in Fig. 1. Each binding conformation results in a symmetric (s) and asymmetric (as) carboxylate stretching vibration. The CH_2 bending mode from the myristic acid alkyl tail overlaps the symmetric stretching region and in this work, we will focus on the asymmetric carboxylate stretching region. We use *ab initio* DFT frequency calculations of carboxylate stretching vibrations on the MSC to assign frequencies to the five binding motifs in the asymmetric carboxylate stretching region.

Our previous work showed that the chelating binding motif is always the lowest energy vibrational frequency in the asymmetric region between 1500 cm^{-1}-1510 cm^{-1}.[58] Similarly, the monodentate binding motif was computationally determined to be one of the highest frequency binding motifs, with peak centers experimentally determined to be around 1580 cm^{-1}. Of the two bridging motifs, the asymmetric stretching mode of *syn-syn* conformation is higher in frequency than that of *syn-anti* due to the electron repulsion of the two syn bonds in the same plane.[59] Thus, in the asymmetric region the frequency order will be: chelating < *syn-anti* < *syn-syn* < monodentate < ionic/dative.

It is worth noting that, in addition to bound carboxylate peaks from 1400 cm^{-1} to 1600 cm^{-1}, the free ligand peaks at 1710 cm^{-1} and 1760 cm^{-1} observed in Fig. 1 can also offer insight on surface ligand equilibrium. Specifically, the free carboxylic acid dimer arises at 1710 cm^{-1} with the monomer at 1760 cm^{-1}.[60,61] We confirm in Fig. S2 of the SI that these peaks are due to desorbed and protonated carboxylic acid species through an equilibrium comparison of the monomeric and dimeric peak areas.

To characterize the bound carboxylate features, we fit the asymmetric stretching region of the FTIR spectrum at 25 °C to five gaussians associated from lowest to highest energy with the

chelating, *syn-anti* bridging, *syn-syn* bridging, monodentate, and dative, as shown in Fig. 1. While at lower temperatures, there is sufficient resolution of the peaks for the spectra to be fit to five gaussians, at higher temperatures, peak broadening increases uncertainty of typical fitting algorithms and is unable to accurately fit the spectrally congested regions of the spectrum as reported by the high variance due to poor fitting. This broadening could be explained in part by the work of Friedfeld et al. that observed a strong endothermic change in a differential scanning calorimetry (DSC) thermogram at 115-130 °C, which they attributed to crystal melting.[34] As the crystal nears the melting temperature at the high end of our temperature range, we would expect higher phonon occupancy and increased geometric disorder that would lead to vibrational linewidth broadening like we observe. As such, a more rigorous method is needed to perform a global fitting and analyze the full temperature FTIR manifold concurrently.

Extracting quantitative information from complicated spectra often necessitates peak fitting to determine the frequency, width, and amplitude of each component in the spectra. For a single spectrum consisting of only a few peaks, this is relatively straightforward to do with a simple non-linear least squares algorithm. In cases where a series of spectra are measured, and certain parameters are not expected to vary across the series, a global fit across the whole series can be performed at the cost of significantly increased complexity. To perform a global fit on the temperature-dependent FTIR spectra reported in this paper, we utilized a Bayesian approach with a MCMC algorithm to sample the parameter space and fit the spectra to a sum of five peaks across all temperatures. Briefly, the use of a Monte Carlo approach allows stochastic sampling of the parameter space, rather than relying on gradient-based methods which may get stuck in local minima.[62] Meanwhile, the use of a constructed Markov Chain satisfying ergodicity and detailed balance ensures the existence of a single stable solution. To quantify how likely a specific set of

parameters is, we turn to Bayes' Theorem to calculate the posterior probability for a particular stochastically sampled fit (Eq. 1).

$$P(\theta|x) = \frac{P(\theta) \cdot P(x|\theta)}{\int P(\theta) \cdot P(x|\theta) d\theta} \quad \textbf{Eq. 1}$$

Where the posterior probability, $P(x)$, represents the probability that a set of parameters, θ, are correct given the observed data, x.[63] This is proportional to the product of the prior probability, $P(\theta)$, which describes the chance of a particular set of parameters occurring using some prior knowledge of the system, multiplied with the likelihood, $P(x|\theta)$, which describes the probability of observing the data given a specific value for the parameters. This product is then normalized to give a probability distribution that integrates to one across the space. Because we are only concerned with finding the maximum posterior probability though, we only need to utilize relative changes in probability and can therefore neglect the computationally expensive integral.

To fit the FTIR spectra reported here, we constructed a model consisting of five gaussian peaks, each with a mean frequency μ_i and a room-temperature width of σ_i. While we assume that the mean vibrational frequencies will not change significantly over the temperature range we probe, as mentioned above, some broadening is observed at elevated temperatures. The exact form of this broadening is too complex to readily model, as it would require a detailed knowledge of the phonon density of states as well as the nature of how the phonon modes affect the ligand binding geometry. Furthermore, trying to account for those behaviors in detail would result in a vastly overparameterized fit. As such, we rely on a simplified power law broadening term that captures the general behavior of the sum width, with each peak following the same broadening parameter, β. The σ_i parameters are treated as constants across temperatures and the width of peak i is then

given by $\sigma_i \left(\frac{T}{T_0}\right)^{\beta}$, with T_0 taken to be 298 K. The full equation for the fit is therefore as follows in Equation 2, where $\tilde{\nu}$ represents the frequency and $c_i(T)$ is the temperature-dependent amplitude for peak i, as discussed in more detail below.

$$f(\tilde{\nu},T) = \sum_{i=1}^{5} c_i(T) e^{\left(-\frac{(\tilde{\nu}-\mu_i)^2}{2\sigma_i^2\left(T/T_0\right)^{2\beta}}\right)} \qquad \textbf{Eq. 2}$$

With the basis of our fit established, we determined appropriate prior distributions through a non-linear least squares fit of the initial room temperature spectrum, as shown in Fig. S3. The MCMC scheme is depicted in Fig. 2a. An ensemble of Monte Carlo walkers is distributed in

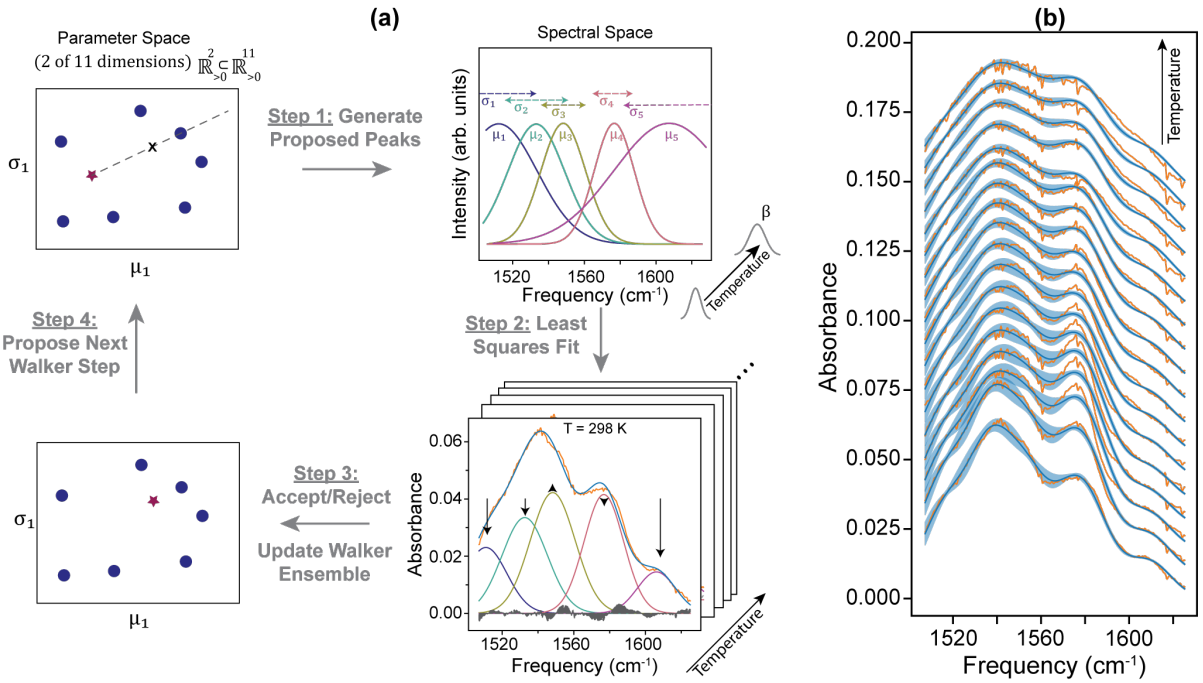

Figure 2. a) Depiction of MCMC global fit process. For a given subset of walkers, stretch moves are randomly generated to propose new positions in parameter space. These new walker positions are used to generate the gaussian peaks corresponding to those parameters of means μ_i and widths σ_i, with a temperature-dependent broadening factor β. These peaks are then fit by least squares to the measured FTIR spectra at each temperature point. The log likelihood of this fit is taken as the negative sum of squared residuals; combined with the prior probabilities of the parameters, the resulting posterior probability is used to stochastically decide whether to accept or reject the new walker positions. The walker ensemble is then updated, and the algorithm iterates to the next subset of walkers and repeats the process. b) Global MCMC fit results (blue lines) for the temperature-dependent InP MSC FTIR spectra (orange lines). The standard deviation across the top 15,000 fits is depicted by the blue shaded area.

Table 1. Extracted parameters from the MCMC global fit on a temperature series of FTIR spectra from an InP MSC sample. Peaks were fit to a gaussian lineshape with position μ_i and width $\sigma_i \left(\frac{T}{T_0}\right)^{\beta}$, as shown in Equation 2. Values and errors are given as means and standard deviations among the sampled points in the top 15,000 posterior probabilities, respectively.

μ_1 (cm^{-1})	σ_1(cm^{-1})	μ_2(cm^{-1})	σ_2(cm^{-1})	μ_3(cm^{-1})	σ_3(cm^{-1})
1515.0 ± 2.1	10.8 ± 1.0	1537.1 ± 1.3	11.2 ± 1.9	1553.9 ± 1.9	9.1 ± 0.8
μ_4(cm^{-1})	σ_4(cm^{-1})	μ_5(cm^{-1})	σ_5(cm^{-1})	β	
1577.0 ± 0.28	12.2 ± 0.27	1609.0 ± 0.28	10.0 ± 0.18	0.62 ± 0.10	

parameter space, and in each MCMC iteration a subset of the walkers is selected and random moves are generated to new proposed positions. The spectral peaks corresponding to these proposed parameters are then constructed, and the temperature-dependent amplitudes are determined by least squares fitting at each temperature point. The fit residuals are evaluated and used to estimate the likelihood function of the parameters. Based on the resulting posterior probability, the moves are then stochastically accepted or rejected and the ensemble positions are updated accordingly. The algorithm iterates through the remaining subsets of walkers and then repeats the process until a preset number of steps have been evaluated. The results of this global fitting process are shown in Fig. 2b, where the data is shown in orange and the average fits are shown by the blue lines with standard deviations at each point given by the blue region. Because we expect the best fit to occur at the maximum posterior probability, we performed statistical analyses on the set of 15,000 sampled points with the highest posterior probabilities. The obtained parameters and their associated uncertainties are shown in Table 1. We note that these values agree closely for a room temperature spectrum with those found previously for MSCs with oleate ligands, which possess a similar carboxylate binding group with a long alkyl tail.[58,60]

From the global fitting results, we can extract amplitude information without needing to enforce any assumptions on the temperature-dependent behavior of the underlying populations.

This allows a more unbiased approach to see how binding motif populations change with temperature. In particular, we can look at the differences of the logs of peak areas to determine whether these populations follow a Boltzmann distribution at any point. This is shown in Fig. 3a as the log area difference with respect to the monodentate binding mode peak, plotted against inverse thermal energy. Above 40 °C (to the left of the black dashed line in the figure) we observe a linear trend to the log area differences, suggesting that a Boltzmann distribution accurately describes the population, as shown in Equation 3. The change in behavior at 40 °C suggests that once there is sufficient thermal energy, the system can fully equilibrate between various binding motifs and dissociated free ligand. This is in line with the previous DSC and ^{13}C NMR work by Friedfeld et al. on these clusters, who observed an endothermic event and linewidth broadening, respectively, occurring at slightly elevated temperatures that they ascribed to ligand rearrangement.[34]

We proceeded to perform linear regressions on the temperature-dependent log area differences in the high-temperature regime. Taking the data above 40 °C for the fits corresponding to the top 15,000 posterior probabilities sampled by the model, we found the averages and standard deviations of the slopes obtained from those regressions. These values are plotted in Fig. 3b. Through application of the Boltzmann equation, we see that the resulting slopes correspond to the relative energy differences between these binding motifs with respect to the monodentate motif, shown by Equation 3.

$$ln(A_{mono}) - ln(A_i) = ln\left(\alpha e^{\Delta\varepsilon/k_BT}\right) = ln(\alpha) + \Delta\varepsilon\frac{1}{k_BT} \qquad \textbf{Eq. 3}$$

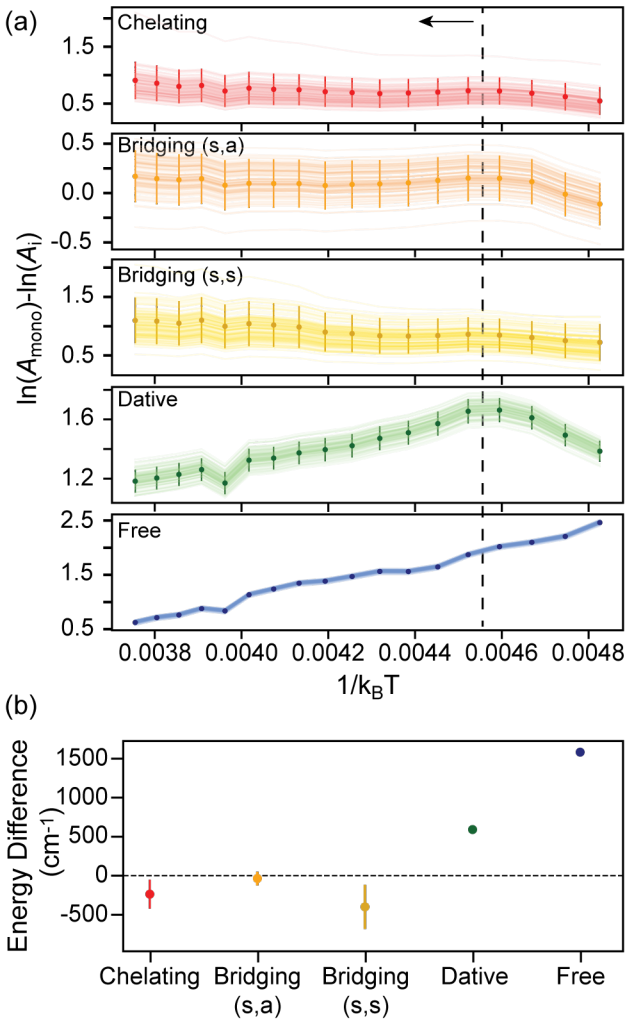

Figure 3. a) Differences of the log of peak areas with respect to the monodentate binding motif, plotted against inverse thermal energy with units of inverse wavenumbers. Markers and error bars represent mean and standard deviation at each temperature point across sampled global fits comprising the top 15,000 posterior probabilities. Lighter lines depict log area differences from the fits corresponding to the 100 highest posterior probabilities. Note the highly correlated error between temperature points which is not conveyed from the error bars alone. While log area differences might vary in magnitude between fits, the temperature trends stay rather consistent. Arrow denotes data points above 40 °C (black dashed line), which demonstrate near linear behavior and were fit using linear regression. b) Extracted slopes from linear regressions of the 45-110 °C regime in panel (a). These values correspond to energy differences relative to the monodentate binding motif, assuming an equilibrated system following Boltzmann statistics. Markers and error bars respectively denote mean and standard deviation of slopes taken from sampled global fits comprising the top 15,000 posterior probabilities.

Where A_i denotes the peak area of component i, $\Delta\varepsilon = \varepsilon_i - \varepsilon_{mono}$ is the change in energy between the two motifs, T is the temperature, k_B is the Boltzmann constant, and α is a proportionality constant.

From Fig. 3b, we can clearly see a varied energy landscape between different binding conformations. While the chelating and *syn-syn* bridging conformations are lower in energy compared to the monodentate motif, the difference is not as large as might be expected from the formation of an additional ligand-metal bond. The energy difference we observe is on the order of 200-400 cm^{-1}, or 0.57-1.14 kcal/mol, far lower than the 15-20 kcal/mol predicted by theory.[52,53] Notably, the *syn-anti* bridging conformation is not significantly different in energy from the monodentate motif, suggesting that the energetic bonus of an additional ligand-metal bond is offset by a confounding factor, potentially such as geometric strain.[64,65] Meanwhile, the dative binding conformation we observe has a higher energy relative to the monodentate. This dative motif is difficult to precisely assign to a geometry; previous single crystal studies show a single ligand in an asymmetric chelating geometry with a bridging dative bond, but these studies were done at -173 °C with phenylacetate ligands and it is unknown whether this preferred geometry will change to a monodentate, dative motif at higher temperatures or with a longer alkyl tail.[44] However, the vibrational energy we observe for this dative binding conformation agrees with general understanding on the increased stability of covalent X-type ligand bonds compared to dative L-type bonding on a cationic surface. Moreover, studies on ruthenium dimer complexes with carboxylic acid ligands have observed similar stretching frequencies for datively bound carboxylic acids that formed hydrogen bonds to neighboring carboxylates.[66] As L-type ligands do not contribute to charge balance on the surface, we would expect them to be able to convert or dissociate more readily like we see here. Finally, we observed a relative energy difference of 1582 ± 19 cm^{-1}, around 4.5 kcal/mol, between the monodentate binding motif and the free ligand. This is of particular note, as this energy is not significantly different from the vibrational frequency, we extract for the monodentate asymmetric stretching mode, 1577.0 ± 0.28 cm^{-1}. These results are

also summarized in Table 2. While these energies do not provide information on the activation barriers between these conformations, they do inform on the relative stability of binding motifs compared to one another. These results suggest that the excitation of this vibrational stretching mode is enough to offset the energy loss associated with ligand dissociation. This is critically relevant for semiconductor nanocrystals where numerous processes, including thermalization to the band edge and Auger-Meitner recombination of trions or multiexcitons, result in energy loss as phonon emission.[67–71] This heat could easily dissipate through the ligand shell resulting in dissociation of the binding group and a decrease in photocatalytic or optical device performance.

Table 2. Summary of relative binding energies extracted from slopes of temperature-dependent log area differences.

Binding Motif	Relative Energy (w.r.t. Monodentate)
Chelating	-236 ± 120 cm^{-1}
Bridging (s,a)	-35 ± 57 cm^{-1}
Bridging (s,s)	-400 ± 184 cm^{-1}
Dative	591 ± 34 cm^{-1}
Free Ligand	1582 ± 19 cm^{-1}

As we have shown, temperature-dependent FTIR spectroscopy provides the capability to directly investigate these evolving populations of ligand binding motifs. In particular, nanocluster platforms offer a well-defined structure and a strictly finite set of possible local surface environments, limiting heterogeneity that could impede interpretation of data obtained using this method. There are numerous other semiconductor clusters whose surface chemistry could be readily probed using this method, including other III-V clusters,[72–74] and the broad range of II-VI clusters of distinct structure and stoichiometry.[75–80] While these measurements were performed in

solution, nanocluster behavior often varies in the solid state. Understanding ligand behavior in device-relevant conditions would be highly advantageous to design principles, and this could be an area of further development to tailor this technique to more disordered solid-state systems, including larger nanocrystals.

CONCLUSION

In this work we have demonstrated that a temperature series of vibrational spectra can be used to measure relative energies of carboxylate binding conformations on the surface of InP magic-sized clusters. A Markov Chain Monte Carlo process can be used to optimize a global fit across all spectra and estimate fit uncertainty. We further show that the relative energy between these binding motifs is much lower than previously thought. A ligand with one bond to the surface is not significantly different in energy from a bidentate ligand bridging two In atoms in a *syn-anti* geometry. Lastly, we demonstrate that the energy difference between a monodentate binding motif and a free ligand is equal to the energy of the monodentate carboxylate asymmetric stretching mode. This suggests that the ligand-functionalized surface of a nanocrystal is far more dynamic and labile than previously thought, and that ligand vibrational excitation has the potential to impact surface binding coverage.

ASSOCIATED CONTENT

The following files are available free of charge: UV-Vis and X-ray diffraction characterization of nanocrystals, analysis of free carboxylic acid dimerization, and comparisons of MCMC results run with various prior distributions (PDF)

AUTHOR INFORMATION

Corresponding Author

*Email: mkhalil@uw.edu

ORCID

Megan D. Klein: 0000-0002-0758-4294

Casey H. Bisted: 0000-0002-0635-3953

Florence Y. Dou: 0000-0002-6780-3321

Jason Sandwisch: 0000-0002-7189-6858

Brandi M. Cossairt: 0000-0002-9891-3259

Munira Khalil: 0000-0002-6508-4124

Author Contributions

The manuscript was written through contributions of all authors. All authors have given approval to the final version of the manuscript. ‡These authors contributed equally.

Notes

ACKNOWLEDGMENT

M.D.K., C.H.B., F.Y.D., J.W.S., B.M.C., and M.K. were supported by a grant from the U.S. Department of Energy, Office of Science, Basic Energy Sciences under Award No: DE-SC0021232. C.H.B. was additionally supported by a National Science Foundation Graduate Research Fellowship under Award No: 1762114. F.Y.D. was additionally supported in part as an educational fellow under National Science Foundation Grant No. DMR-2019444.

ABBREVIATIONS

MCMC, Markov Chain Monte Carlo; FTIR, Fourier transform infrared; MSC, magic-sized cluster; NC, nanocrystals

REFERENCES

(1) Won, Y.-H.; Cho, O.; Kim, T.; Chung, D.-Y.; Kim, T.; Chung, H.; Jang, H.; Lee, J.; Kim, D.; Jang, E. Highly Efficient and Stable InP/ZnSe/ZnS Quantum Dot Light-Emitting Diodes. *Nature* **2019**, *575* (7784), 634–638.

(2) Jang, E.; Kim, Y.; Won, Y.-H.; Jang, H.; Choi, S.-M. Environmentally Friendly InP-Based Quantum Dots for Efficient Wide Color Gamut Displays. *ACS Energy Lett.* **2020**, *5* (4), 1316–1327.

(3) le Feber, B.; Prins, F.; De Leo, E.; Rabouw, F. T.; Norris, D. J. Colloidal-Quantum-Dot Ring Lasers with Active Color Control. *Nano Lett.* **2018**, *18* (2), 1028–1034.

(4) Park, Y.-S.; Roh, J.; Diroll, B. T.; Schaller, R. D.; Klimov, V. I. Colloidal Quantum Dot Lasers. *Nature Reviews Materials* **2021**, *6* (5), 382–401.

(5) Roh, J.; Park, Y.-S.; Lim, J.; Klimov, V. I. Optically Pumped Colloidal-Quantum-Dot Lasing in LED-like Devices with an Integrated Optical Cavity. *Nat. Commun.* **2020**, *11* (1), 271.

(6) Coropceanu, I.; Bawendi, M. G. Core/Shell Quantum Dot Based Luminescent Solar Concentrators with Reduced Reabsorption and Enhanced Efficiency. *Nano Lett.* **2014**, *14* (7), 4097–4101.

(7) Wu, K.; Li, H.; Klimov, V. I. Tandem Luminescent Solar Concentrators Based on Engineered Quantum Dots. *Nat. Photonics* **2018**, *12* (2), 105–110.

(8) You, Y.; Tong, X.; Wang, W.; Sun, J.; Yu, P.; Ji, H.; Niu, X.; Wang, Z. M. Eco-Friendly Colloidal Quantum Dot-Based Luminescent Solar Concentrators. *Adv. Sci.* **2019**, *6* (9), 1801967.

(9) Pearce, O. M.; Duncan, J. S.; Damrauer, N. H.; Dukovic, G. Ultrafast Hole Transfer from CdS Quantum Dots to a Water Oxidation Catalyst. *J. Phys. Chem. C* **2018**, *122* (30), 17559–17565.

(10) Weiss, E. A. Designing the Surfaces of Semiconductor Quantum Dots for Colloidal Photocatalysis. *ACS Energy Lett.* **2017**, *2* (5), 1005–1013.

(11) Kwon, H.; Kim, S.; Kang, S. B.; Bang, J. Preparation of InP Quantum Dots-TiO 2 Nanoparticle Composites with Enhanced Visible Light Induced Photocatalytic Activity. *CrystEngComm* **2022**, *24* (20), 3724–3730.

(12) Chakraborty, I. N.; Roy, S.; Devatha, G.; Rao, A.; Pillai, P. P. InP/ZnS Quantum Dots as Efficient Visible-Light Photocatalysts for Redox and Carbon–Carbon Coupling Reactions. *Chem. Mater.* **2019**, *31* (7), 2258–2262.

(13) Ricci, F.; Marougail, V.; Varnavski, O.; Wu, Y.; Padgaonkar, S.; Irgen-Gioro, S.; Weiss, E. A.; Goodson, T., 3rd. Enhanced Exciton Quantum Coherence in Single CsPbBr3 Perovskite Quantum Dots Using Femtosecond Two-Photon Near-Field Scanning Optical Microscopy. *ACS Nano* **2021**. 15(8),12955-12965.

(14) Utzat, H.; Sun, W.; Kaplan, A. E. K.; Krieg, F.; Ginterseder, M.; Spokoyny, B.; Klein, N. D.; Shulenberger, K. E.; Perkinson, C. F.; Kovalenko, M. V.; et al. Coherent Single-Photon Emission from Colloidal Lead Halide Perovskite Quantum Dots. *Science* **2019**, *363* (6431), 1068–1072.

(15) Chen, Y.; Sharp, D.; Saxena, A.; Nguyen, H.; Cossairt, B. M.; Majumdar, A. Integrated Quantum Nanophotonics with Solution-processed Materials. *Adv. Quantum Technol.* **2022**, *5* (1), 2100078.

(16) Schnitzenbaumer, K. J.; Labrador, T.; Dukovic, G. Impact of Chalcogenide Ligands on Excited State Dynamics in CdSe Quantum Dots. *J. Phys. Chem. C* **2015**, *119* (23), 13314–13324.

(17) Van Der Stam, W.; Du Fossé, I.; Grimaldi, G.; Monchen, J. O. V.; Kirkwood, N.; Houtepen, A. J. Spectroelectrochemical Signatures of Surface Trap Passivation on CdTe Nanocrystals. *Chem. Mater.* **2018**, *30* (21), 8052–8061.

(18) Houtepen, A. J.; Hens, Z.; Owen, J. S.; Infante, I. On the Origin of Surface Traps in Colloidal II-VI Semiconductor Nanocrystals. *Chem. Mater.* **2017**, *29* (2), 752–761.

(19) Hughes, K. E.; Stein, J. L.; Friedfeld, M. R.; Cossairt, B. M.; Gamelin, D. R. Effects of Surface Chemistry on the Photophysics of Colloidal InP Nanocrystals. *ACS Nano* **2019**, *13* (12), 14198–14207.

(20) Xiao, P.; Zhang, Z.; Ge, J.; Deng, Y.; Chen, X.; Zhang, J.-R.; Deng, Z.; Kambe, Y.; Talapin, D. V.; Wang, Y. Surface Passivation of Intensely Luminescent All-Inorganic Nanocrystals and Their Direct Optical Patterning. *Nat. Commun.* **2023**, *14* (1), 49.

(21) Ge, J.; Liang, J.; Chen, X.; Deng, Y.; Xiao, P.; Zhu, J.-J.; Wang, Y. Designing Inorganically Functionalized Magic-Size II-VI Clusters and Unraveling Their Surface States. *Chem. Sci.* **2022**, *13* (40), 11755–11763.
(22) Kirkwood, N.; Monchen, J. O. V.; Crisp, R. W.; Grimaldi, G.; Bergstein, H. A. C.; du Fossé, I.; van der Stam, W.; Infante, I.; Houtepen, A. J. Finding and Fixing Traps in II-VI and III-V Colloidal Quantum Dots: The Importance of Z-Type Ligand Passivation. *J. Am. Chem. Soc.* **2018**, *140* (46), 15712–15723.
(23) Dolai, S.; Nimmala, P. R.; Mandal, M.; Muhoberac, B. B.; Dria, K.; Dass, A.; Sardar, R. Isolation of Bright Blue Light-Emitting CdSe Nanocrystals with 6.5 KDa Core in Gram Scale: High Photoluminescence Efficiency Controlled by Surface Ligand Chemistry. *Chem. Mater.* **2014**, *26* (2), 1278–1285.
(24) Anderson, N. C.; Hendricks, M. P.; Choi, J. J.; Owen, J. S. Ligand Exchange and the Stoichiometry of Metal Chalcogenide Nanocrystals: Spectroscopic Observation of Facile Metal-Carboxylate Displacement and Binding. *J. Am. Chem. Soc.* **2013**, *135* (49), 18536–18548.
(25) Busby, E.; Anderson, N. C.; Owen, J. S.; Sfeir, M. Y. Effect of Surface Stoichiometry on Blinking and Hole Trapping Dynamics in CdSe Nanocrystals. *J. Phys. Chem. C* **2015**, *119* (49), 27797–27803.
(26) Hartley, C. L.; Kessler, M. L.; Dempsey, J. L. Molecular-Level Insight into Semiconductor Nanocrystal Surfaces. *J. Am. Chem. Soc.* **2021**, *143* (3), 1251–1266.
(27) Owen, J. Nanocrystal Structure. The Coordination Chemistry of Nanocrystal Surfaces. *Science* **2015**, *347* (6222), 615–616.
(28) Weiss, E. A. Organic Molecules as Tools to Control the Growth, Surface Structure, and Redox Activity of Colloidal Quantum Dots. *Acc. Chem. Res.* **2013**, *46* (11), 2607–2615.
(29) Eagle, F. W.; Park, N.; Cash, M.; Cossairt, B. M. Surface Chemistry and Quantum Dot Luminescence: Shell Growth, Atomistic Modification, and Beyond. *ACS Energy Letters* **2021**, *6* (3), 977–984.
(30) Green, M. L. H. A New Approach to the Formal Classification of Covalent Compounds of the Elements. *J. Organomet. Chem.* **1995**, *500* (1–2), 127–148.
(31) Owen, J. S.; Park, J.; Trudeau, P. E.; Alivisatos, A. P. Reaction Chemistry and Ligand Exchange at Cadmium-Selenide Nanocrystal Surfaces. *J. Am. Chem. Soc.* **2008**, *130* (37), 12279–12281.
(32) De Roo, J.; De Keukeleere, K.; Hens, Z.; Van Driessche, I. From Ligands to Binding Motifs and beyond; the Enhanced Versatility of Nanocrystal Surfaces. *Dalton Trans.* **2016**, *45* (34), 13277–13283.
(33) Calvin, J. J.; Ben-Moshe, A.; Curling, E. B.; Brewer, A. S.; Sedlak, A. B.; Kaufman, T. M.; Alivisatos, A. P. Thermodynamics of the Adsorption of Cadmium Oleate to Cadmium Sulfide Quantum Dots and Implications of a Dynamic Ligand Shell. *J. Phys. Chem. C* **2022**, 126 (30), 12958-12971.
(34) Friedfeld, M. R.; Johnson, D. A.; Cossairt, B. M. Conversion of InP Clusters to Quantum Dots. *Inorg. Chem.* **2019**, *58* (1), 803–810.
(35) Fritzinger, B.; Capek, R. K.; Lambert, K.; Martins, J. C.; Hens, Z. Utilizing Self-Exchange to Address the Binding of Carboxylic Acid Ligands to CdSe Quantum Dots. *J. Am. Chem. Soc.* **2010**, *132* (29), 10195–10201.
(36) Calvin, J. J.; O'Brien, E. A.; Sedlak, A. B.; Balan, A. D.; Alivisatos, A. P. Thermodynamics of Composition Dependent Ligand Exchange on the Surfaces of Colloidal Indium Phosphide Quantum Dots. *ACS Nano* **2021**, *15* (1), 1407–1420.
(37) Elimelech, O.; Aviv, O.; Oded, M.; Banin, U. A Tale of Tails: Thermodynamics of CdSe Nanocrystal Surface Ligand Exchange. *Nano Lett.* **2020**, *20* (9), 6396–6403.
(38) Anderson, N. C.; Owen, J. S. Soluble, Chloride-Terminated CdSe Nanocrystals: Ligand Exchange Monitored by 1H and 31P NMR Spectroscopy. *Chem. Mater.* **2013**, *25* (1), 69–76.
(39) Drijvers, E.; De Roo, J.; Martins, J. C.; Infante, I.; Hens, Z. Ligand Displacement Exposes Binding Site Heterogeneity on CdSe Nanocrystal Surfaces. *Chem. Mater.* **2018**, *30* (3), 1178–1186.

(40) Stelmakh, A.; Aebli, M.; Baumketner, A.; Kovalenko, M. V. On the Mechanism of Alkylammonium Ligands Binding to the Surface of CsPbBr3Nanocrystals. *Chem. Mater.* **2021**, *33* (15), 5962–5973.
(41) Ritchhart, A.; Cossairt, B. M. Quantifying Ligand Exchange on InP Using an Atomically Precise Cluster Platform. *Inorg. Chem.* **2019**, *58* (4), 2840–2847.
(42) Knauf, R. R.; Lennox, J. C.; Dempsey, J. L. Quantifying Ligand Exchange Reactions at CdSe Nanocrystal Surfaces. *Chem. Mater.* **2016**, *28* (13), 4762–4770.
(43) Kessler, M. L.; Starr, H. E.; Knauf, R. R.; Rountree, K. J.; Dempsey, J. L. Exchange Equilibria of Carboxylate-Terminated Ligands at PbS Nanocrystal Surfaces. *Phys. Chem. Chem. Phys.* **2018**, *20* (36), 23649–23655.
(44) Gary, D. C.; Flowers, S. E.; Kaminsky, W.; Petrone, A.; Li, X.; Cossairt, B. M. Single-Crystal and Electronic Structure of a 1.3 Nm Indium Phosphide Nanocluster. *J. Am. Chem. Soc.* **2016**, *138* (5), 1510–1513.
(45) Zhao, Q.; Kulik, H. J. Electronic Structure Origins of Surface-Dependent Growth in III–V Quantum Dots. *Chem. Mater.* **2018**, *30* (20), 7154–7165.
(46) Rempel, J. Y.; Trout, B. L.; Bawendi, M. G.; Jensen, K. F. Density Functional Theory Study of Ligand Binding on CdSe (0001), (0001), and (1120) Single Crystal Relaxed and Reconstructed Surfaces: Implications for Nanocrystalline Growth. *J. Phys. Chem. B* **2006**, *110* (36), 18007–18016.
(47) Puzder, A.; Williamson, A. J.; Zaitseva, N.; Galli, G.; Manna, L.; Alivisatos, A. P. The Effect of Organic Ligand Binding on the Growth of CdSe Nanoparticles Probed by Ab Initio Calculations. *Nano Lett.* **2004**, *4* (12), 2361–2365.
(48) Cass, L. C.; Malicki, M.; Weiss, E. A. The Chemical Environments of Oleate Species within Samples of Oleate-Coated PbS Quantum Dots. *Anal. Chem.* **2013**, *85* (14), 6974–6979.
(49) Cros-Gagneux, A.; Delpech, F.; Nayral, C.; Cornejo, A.; Coppel, Y.; Chaudret, B. Surface Chemistry of InP Quantum Dots: A Comprehensive Study. *J. Am. Chem. Soc.* **2010**, *132* (51), 18147–18157.
(50) Nguyen, K. A.; Pachter, R.; Day, P. N. Systematic Study of the Properties of CdS Clusters with Carboxylate Ligands Using a Deep Neural Network Potential Developed with Data from Density Functional Theory Calculations. *J. Phys. Chem. A* **2020**, *124* (50), 10472–10481.
(51) Bealing, C. R.; Baumgardner, W. J.; Choi, J. J.; Hanrath, T.; Hennig, R. G. Predicting Nanocrystal Shape through Consideration of Surface-Ligand Interactions. *ACS Nano* **2012**, *6* (3), 2118–2127.
(52) Xie, L.; Zhao, Q.; Jensen, K. F.; Kulik, H. J. Direct Observation of Early-Stage Quantum Dot Growth Mechanisms with High-Temperature Ab Initio Molecular Dynamics. *J. Phys. Chem. C* **2016**, *120* (4), 2472–2483.
(53) Zhang, J.; Zhang, H.; Cao, W.; Pang, Z.; Li, J.; Shu, Y.; Zhu, C.; Kong, X.; Wang, L.; Peng, X. Identification of Facet-Dependent Coordination Structures of Carboxylate Ligands on CdSe Nanocrystals. *J. Am. Chem. Soc.* **2019**, *141* (39), 15675–15683.
(54) Foreman-Mackey, D.; Hogg, D. W.; Lang, D.; Goodman, J. Emcee: The MCMC Hammer. *PASP* **2013**, *125* (925), 306.
(55) Goodman, J.; Weare, J. Ensemble Samplers with Affine Invariance. *Communications in Applied Mathematics and Computational Science* **2010**, *5* (1), 65–80.
(56) Boles, M. A.; Ling, D.; Hyeon, T.; Talapin, D. V. The Surface Science of Nanocrystals. *Nat. Mater.* **2016**, *15* (2), 141–153.
(57) Gary, D. C.; Petrone, A.; Li, X.; Cossairt, B. M. Investigating the Role of Amine in InP Nanocrystal Synthesis: Destabilizing Cluster Intermediates by Z-Type Ligand Displacement. *Chem. Commun.* **2016**, *53* (1), 161–164.
(58) Leger, J. D.; Friedfeld, M. R.; Beck, R. A.; Gaynor, J. D.; Petrone, A.; Li, X.; Cossairt, B. M.; Khalil, M. Carboxylate Anchors Act as Exciton Reporters in 1.3 Nm Indium Phosphide Nanoclusters. *J. Phys. Chem. Lett.* **2019**, *10* (8), 1833–1839.
(59) Zeleňák, V.; Vargová, Z.; Györyová, K. Correlation of Infrared Spectra of Zinc(II) Carboxylates with Their Structures. *Spectrochim. Acta A Mol. Biomol. Spectrosc.* **2007**, *66* (2), 262–272.
(60) Taheri, P.; Wielant, J.; Hauffman, T.; Flores, J. R.; Hannour, F.; De Wit, J. H. W.; Mol, J. M. C.;

Terryn, H. A Comparison of the Interfacial Bonding Properties of Carboxylic Acid Functional Groups on Zinc and Iron Substrates. *Electrochim. Acta* **2011**, *56* (4), 1904–1911.
(61) Socrates, G. *Infrared and Raman Characteristic Group Frequencies: Tables and Charts*; John Wiley & Sons, 2004.
(62) Ashner, M. N.; Winslow, S. W.; Swan, J. W.; Tisdale, W. A. Markov Chain Monte Carlo Sampling for Target Analysis of Transient Absorption Spectra. *J. Phys. Chem. A* **2019**, *123* (17), 3893–3902.
(63) LII. An Essay towards Solving a Problem in the Doctrine of Chances. By the Late Rev. Mr. Bayes, F. R. S. Communicated by Mr. Price, in a Letter to John Canton, A. M. F. R. S. *Philosophical Transactions of the Royal Society of London* **1763**, *53*, 370–418.
(64) Hemmert, C.; Verelst, M.; Tuchagues, J.-P. Pentadentate Dinucleating Ligands Affording Bis(μ-Carboxylato- O , O ′)Diiron(II) Complexes. *Chem. Commun.* **1996**, *0* (5), 617–618.
(65) Su, E.; Guven, A.; Kani, I. Oxygen Bridged Homobinuclear Mn(II) Compounds with Anthranilic Acid: Theoretical Calculations, Oxidation and Catalase Activity. *Appl. Organomet. Chem.* **2018**, *32* (2), e4105.
(66) Rotem, M.; Goldberg, I.; Shmueli, U.; Shvo, Y. Chemistry of Bridged Carboxylate Ruthenium Complexes. Crystal Structures of [Ru(PhCOO)(CO)2(PhCOOH]2, [Ru(4-FC6H4COO)2(CO)5(H2O)]2·0.5 C6H6, and [Ru2(s-BuCO2)2(CO)4(s-BuCO2H)]2. *J. Organomet. Chem.* **1986**, *314* (1), 185–212.
(67) Kambhampati, P. Hot Exciton Relaxation Dynamics in Semiconductor Quantum Dots: Radiationless Transitions on the Nanoscale. *J. Phys. Chem. C* **2011**, *115* (45), 22089–22109.
(68) Auger, P. Sur les rayons β secondaires produits dans un gaz par des rayons X. *C.R.A.S.* **1923**,177, ,169-171.
(69) Meitner, L. Über Den Zusammenhang Zwischen β- Und γ-Strahlen. *Zeitschrift für Physik* **1922**, *9* (1), 145–152.
(70) Matsakis, D.; Coster, A.; Laster, B.; Sime, R. A Renaming Proposal: "The Auger–Meitner Effect." *Phys. Today* **2019**, *72* (9), 10–11.
(71) Guyot-Sionnest, P.; Shim, M.; Matranga, C.; Hines, M. Intraband Relaxation in CdSe Quantum Dots. *Phys. Rev. B Condens. Matter* **1999**, *60* (4), R2181–R2184.
(72) Ritchhart, A.; Cossairt, B. M. Templated Growth of InP Nanocrystals with a Polytwistane Structure. *Angew. Chem. Weinheim Bergstr. Ger.* **2018**, *130* (7), 1926–1930.
(73) Kwon, Y.; Oh, J.; Lee, E.; Lee, S. H.; Agnes, A.; Bang, G.; Kim, J.; Kim, D.; Kim, S. Evolution from Unimolecular to Colloidal-Quantum-Dot-like Character in Chlorine or Zinc Incorporated InP Magic Size Clusters. *Nat. Commun.* **2020**, *11* (1), 3127.
(74) Kwon, Y.; Kim, S. Indium Phosphide Magic-Sized Clusters: Chemistry and Applications. *NPG Asia Materials* **2021**, *13* (1), 1–16.
(75) Cossairt, B. M.; Owen, J. S. CdSe Clusters: At the Interface of Small Molecules and Quantum Dots. *Chem. Mater.* **2011**, *23* (12), 3114–3119.
(76) Kilina, S.; Ivanov, S.; Tretiak, S. Effect of Surface Ligands on Optical and Electronic Spectra of Semiconductor Nanoclusters. *J. Am. Chem. Soc.* **2009**, *131* (22), 7717–7726.
(77) Soloviev, V. N.; Eichhöfer, A.; Fenske, D.; Banin, U. Size-Dependent Optical Spectroscopy of a Homologous Series of CdSe Cluster Molecules. *J. Am. Chem. Soc.* **2001**, *123* (10), 2354–2364.
(78) Swenson, N. K.; Ratner, M. A.; Weiss, E. A. Computational Study of the Influence of the Binding Geometries of Organic Ligands on the Photoluminescence Quantum Yield of CdSe Clusters. *J. Phys. Chem. C* **2016**, *120* (12), 6859–6868.
(79) Mule, A. S.; Mazzotti, S.; Rossinelli, A. A.; Aellen, M.; Prins, P. T.; van der Bok, J. C.; Solari, S. F.; Glauser, Y. M.; Kumar, P. V.; Riedinger, A.; et al. Unraveling the Growth Mechanism of Magic-Sized Semiconductor Nanocrystals. *J. Am. Chem. Soc.* **2021**, *143* (4), 2037–2048.
(80) Bootharaju, M. S.; Baek, W.; Lee, S.; Chang, H.; Kim, J.; Hyeon, T. Magic-Sized Stoichiometric II-VI Nanoclusters. *Small* **2021**, *17* (27), e2002067.

TOC Graphic